Title	Fluid-structure interaction effects on attitude stability of an inflatable aerodecelerator
Author(s)	Fujita, Yosuke; Saha, Sanjoy Kumar; Takahashi, Yusuke et al.
Citation	Physics of fluids, 37(6), 067161 https://doi.org/10.1063/5.0272358
Issue Date	2025-06-30
Doc URL	https://hdl.handle.net/2115/97945
Rights	This article may be downloaded for personal use only. Any other use requires prior permission of the author and AIP Publishing. This article appeared in Yosuke Fujita, Sanjoy Kumar Saha, Yusuke Takahashi, Kazuhiko Yamada; Fluid-structure interaction effects on attitude stability of an inflatable aerodecelerator. Physics of Fluids 1 June 2025; 37 (6): 067161 and may be found at https://doi.org/10.1063/5.0272358.
Type	journal article
File Information	067161_1_5.0272358.pdf

RESEARCH ARTICLE | JUNE 30 2025

Fluid–structure interaction effects on attitude stability of an inflatable aerodecelerator

Yosuke Fujita (藤田耀介) ; Sanjoy Kumar Saha (サハサンジョイクマー) ; Yusuke Takahashi (高橋裕介) ; Kazuhiko Yamada (山田和彦)

Physics of Fluids 37, 067161 (2025)
https://doi.org/10.1063/5.0272358

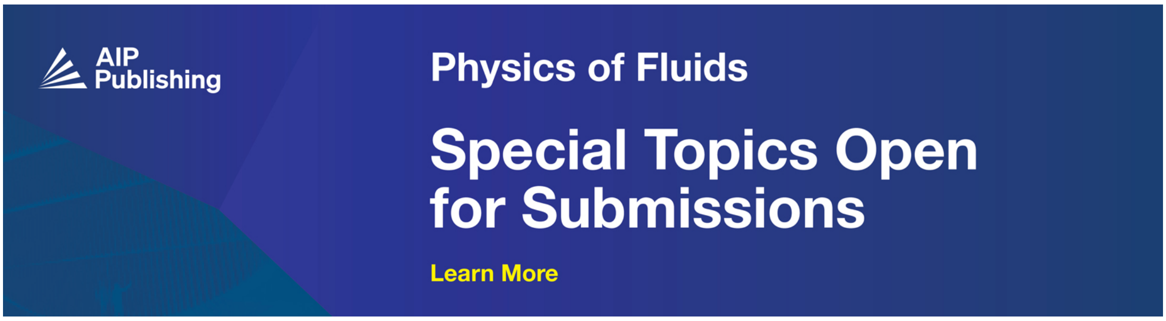

Fluid–structure interaction effects on attitude stability of an inflatable aerodecelerator

Cite as: Phys. Fluids **37**, 067161 (2025); doi: 10.1063/5.0272358
Submitted: 24 March 2025 · Accepted: 7 May 2025 ·
Published Online: 30 June 2025

View Online Export Citation CrossMark

Yosuke Fujita (藤田耀介),[1] Sanjoy Kumar Saha (サハサンジョイクマー),[1] Yusuke Takahashi (高橋裕介),[2,a)] and Kazuhiko Yamada (山田和彦)[3]

AFFILIATIONS

[1]Graduate School of Engineering, Hokkaido University, Kita 13 Nishi 8, Kita-ku, Sapporo 060-8628, Hokkaido, Japan
[2]Faculty of Engineering, Hokkaido University, Kita 13 Nishi 8, Kita-ku, Sapporo 060-8628, Hokkaido, Japan
[3]Institute of Space and Astronautical Science, Japan Aerospace Exploration Agency, 3-1-1 Yoshinodai, Chuo-ku, Sagamihara 252-5210, Kanagawa, Japan

[a)]Author to whom correspondence should be addressed: ytakahashi@eng.hokudai.ac.jp

ABSTRACT

As a new atmospheric-entry technology, the research and development of atmospheric-entry vehicles with flexible aeroshells has been rapidly expanding. A lightweight and large-area flexible aeroshell enables a low-ballistic coefficient of flight and an efficient aerodynamic deceleration, thereby reducing aerodynamic heating and communication blackouts. Aerodynamic forces deform flexible aeroshells, altering their aerodynamic characteristics. However, the manner in which the attitude characteristics change when the aeroshell undergoes significant shape deformation is not well understood. In this study, the attitude and aerodynamic characteristics of a flexible aeroshell were clarified using wind tunnel tests at a given angle of attack and corresponding fluid–structure interaction (FSI) analysis. The FSI analysis method is based on a partitioned coupling method for large-scale parallel computers that use open-source software. The FSI analytical model reasonably explained the aeroshell deformation and aerodynamic coefficient behavior, and its validity was confirmed by wind tunnel experiments. The shape deformation of the flexible aeroshell weakened its restoring motion, thus exhibiting attitude instability compared with those prior to deformation.

I. INTRODUCTION

Atmospheric-entry capsules with flexible aeroshells have undergone significant advancements in recent years, particularly for missions such as sample return from orbit. Increasing interest in planetary exploration, particularly on Mars, has led to a growing demand for larger aeroshells to accommodate the unique challenges of entry into low-density atmospheres. Along with advancements in data recovery system designs using sounding rockets and the exploration of space utilization through Earth's atmospheric entry, these developments have highlighted the need for more efficient and scalable aeroshell designs.

Flexible aeroshell technology is regarded as a promising approach to reducing aerodynamic heating during atmospheric entry, particularly through the use of inflatable structures. The inflatable reentry vehicle experiment (IRVE)[1–3] and the hypersonic inflatable aerodynamic decelerator (HIAD),[4] both featuring large stacked-torus-type inflatable systems, have been developed as representative examples of this approach. In parallel, a flare-type, thin-membrane configuration has also been considered a promising design and is being developed as the membrane aeroshell for atmospheric-entry capsule (MAAC).[5] A suborbital demonstration of this configuration was conducted in 2012 during the quasi-orbital entry experiment known as the sounding rocket experiment of MAAC (SMAAC).[6] Further progress was made in 2021, when MAAC technology was used in the reentry and recovery module with deployable aeroshell technology for sounding rocket experiments (RATS).[7,8]

A schematic of the MAAC-type aeroshell configuration is shown in Fig. 1. It consists of a rigid capsule, an inflatable torus, and a thin-membrane aeroshell connecting the two. While the capsule itself is rigid, both the torus and the membrane are made of ZYLON fabric, making them lightweight and highly flexible. The torus retains its shape by maintaining internal gas pressure. During transport, such as when mounted on a rocket, the torus and membrane can be compactly folded, which is advantageous given the strict constraints on payload volume. Once in orbit, gas is injected into the torus to deploy the aeroshell. At this stage, the configuration achieves a low-ballistic coefficient

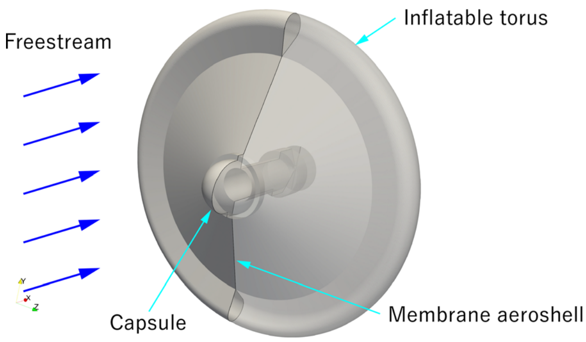

FIG. 1. Flare-type thin-membrane flexible aeroshell.

due to its low mass and large surface area, allowing for efficient aerodynamic deceleration at high altitudes. This reduces both aerodynamic heating during atmospheric entry and terminal velocity, thereby enabling a parachute-free landing capability.

Significant deformation of the flexible aeroshell due to aerodynamic forces was observed in a flight demonstration test.[6] Such shape deformation affects both the aerodynamic forces and aerodynamic heating. Takahashi *et al.*[9,10] investigated the impact of structural deformation on the aerodynamic force and heating of the SMAAC vehicle. These studies revealed that deformation alters the shock wave structure and heat load on the aeroshell at supersonic conditions. Clark *et al.*[11] investigated the aerodynamic characteristics and fluid–structure interaction (FSI) behavior of a tension-cone inflatable aerodynamic decelerator through wind tunnel tests at supersonic speeds. Kramer *et al.*[12] numerically demonstrated that the resonance phenomena of the tension-cone-type aeroshell, caused by the coupled interaction between the aeroshell and surrounding flow, can induce large non-axisymmetric oscillations of the aeroshell. Wu *et al.*[13] studied the static and dynamic aeroelastic characteristics of a stacked-tori inflatable aeroshell at supersonic and transonic speeds and showed that low-frequency oscillations occur under conditions with an angle of attack. Hollis *et al.*[14] clarified the surface deflection effect on boundary-layer transition and surface heating distribution for a HIAD wind tunnel model in a hypersonic flow at a Mach number of 6. Takahashi *et al.*[15] demonstrated that structural deformation of a flexible aeroshell during atmospheric entry at an altitude of 88.4 km significantly affects the heat flux distribution, using a one-way coupled FSI method.

Flight demonstrations using SMAAC and RATS have indicated that aerodynamic attitude instability occurs at subsonic speeds.[16] This is believed to be due to dynamic attitude instability, that is, the divergence of the attitude motion. Attitude instability in rigid aeroshell capsules has also become a significant issue. Hiraki[17] and Koga *et al.*[18] conducted experimental studies on conventional rigid capsules, such as those used in the Hayabusa and HTV small reentry missions. Takasawa *et al.*[19] studied the static attitude stability of a deep-space sample return capsule (DS-SRC) with thin aeroshell capsules. This study suggests that, at all angles of attack, the thin aeroshell capsule is statically stabilized by the pressure difference between the forward and rear sides, regardless of the position of the center of gravity. Takasawa *et al.*[20] also investigated dynamic attitude instability. Moreover, wind tunnel tests of the DS-SRC in single degrees of freedom revealed that the moment of inertia of the vehicle affects the time required for the vehicle to reach the limit cycle oscillation (LCO) and the amplitude at the LCO.

Previous studies have shown that the attitude instability of rigid capsules is partly due to the phase delay of the wake. However, for flexible aeroshell capsules, particularly the thin-membrane aeroshells used in SMAAC and RATS, it remains unclear how the coupled behavior between the flexible structure and the fluid further affects attitude instability. Numerical simulation is one of the effective tools for investigating FSI behavior. Saha *et al.*[21] investigated the aerodynamic characteristics of a flexible aeroshell at an angle of attack of 0°; however, they did not discuss cases at nonzero angles of attack, and the FSI characteristics related to vehicle attitude remain unexplored. To ensure successful atmospheric entry using flexible aeroshells, it is necessary to clarify the aerodynamic characteristics relevant to vehicle attitude, including FSI effects, and to ensure attitude stability even at subsonic speeds. Saha *et al.*[22] proposed an FSI aeroelasticity simulation model in the transonic regime. Takahashi[23] and Saha *et al.*[24] proposed methods for identifying dominant displacement modes in FSI and examined how aerodynamic forces influence these modes and their frequencies. To accurately predict the structural behavior of flexible aeroshells, it is essential to appropriately model geometric and material properties. However, this is not straightforward and involves tradeoffs with computational cost as well as challenges related to validation. Even when using simplified models, validation against experimental data remains critical.

The purpose of this study was to clarify the attitude characteristics of a flexible aeroshell by conducting wind tunnel tests and FSI analyses at a given angle of attack. The analytical model was validated by comparison with results from wind tunnel tests and FSI simulations. The remainder of this paper is organized as follows. Section II describes the wind tunnel test, Sec. III describes the FSI analysis method, Sec. IV presents the results and discussion, and Sec. V concludes the paper.

II. WIND TUNNEL EXPERIMENT

A. Transonic wind tunnel

A transonic wind tunnel at the Institute of Space and Astronautical Science (ISAS) of the Japan Aerospace Exploration Agency was used to evaluate the aerodynamic properties of flexible aeroshells.[25] The wind tunnel is a blowdown type, with a Mach number range of 0.3–1.3. The measurement section was a square channel with dimensions $600 \times 600\,\text{mm}^2$. The walls of the measurement section were perforated to reduce wall effects. The sting that holds the experimental model in place is movable, allowing the angle of attack to be changed within a range of $\pm 15°$.

B. Experimental setup

A schematic of the experimental model used in the wind tunnel test is shown in Fig. 2. In this study, the x axis is defined to coincide with the body axis (longitudinal direction of the model), with the y- and z axes defined as orthogonal to it.

Figure 3(a) shows the flexible aeroshell model. The thin aeroshell of the flexible model was made of Zylon fabric (LZY0160W, Toyobo Co., Ltd.),[26] which was also used in the SMAAC vehicle, and the torus part was an aluminum ring simulating an inflatable torus. The capsule head was made of stainless steel and had a diameter of 12 mm, the aluminum ring had an outer diameter of 80 mm, the tube diameter was

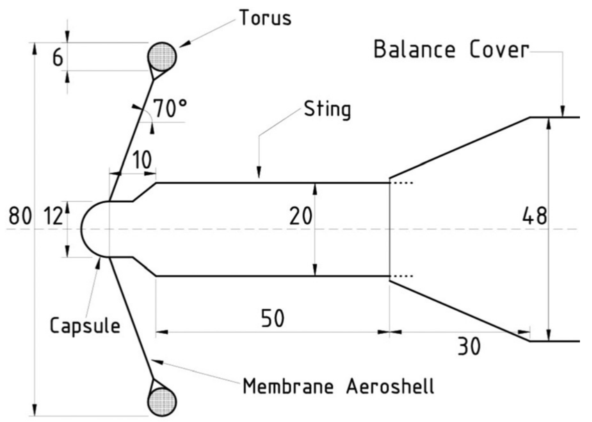

FIG. 2. Schematic of the experimental model (dimensions in millimeters).

6 mm, and the thickness of the Zylon fabric—the material of the thin aeroshell—was approximately 0.1 mm. The Zylon fabric was sewn onto an aluminum ring using a sewing machine and hand. The flare angle of the aeroshell was 70°, which was identical to that of the SMAAC vehicle.

Figure 3(b) shows the rigid aeroshell model. The rigid aeroshell model had almost the same shape as the flexible aeroshell model before deformation, with an outer diameter of 80 mm and a flare angle of 70°. A rigid model was constructed using a 3D printer (Form2, Formlabs) from gray resin V4. To strengthen the rigid model, the aeroshell was thickened in the backward direction to a thickness of 1.88 mm.

C. Measurement system

Aerodynamic 6-component forces were measured by using an internal balance attached to the interior of the sting. The balance cover was attached 66 mm behind the capsule head, and aerodynamic forces were measured in the sting and aeroshell sections. The center of measurement of the internal balance was 238.5 mm from the capsule head. The aerodynamic coefficients were calculated by non-dimensionalizing the forces and moments measured by the balance. The aerodynamic coefficients were calculated by normalizing the measured forces and moments using the projected area of the aeroshell ($5027\ mm^2$) as the characteristic area and the aeroshell diameter (80 mm) as the characteristic length. The balance employed in the wind tunnel had a time resolution of 1000 Hz. Pressure tubes were placed at 90° intervals to measure the pressure at the back of the aeroshell, as shown in Fig. 4. The sampling frequency of the pressure tube was 1000 Hz. Piezoelectric films (Piezo Film Vibra Tab, SKU 605-00004, Parallax Inc.)[27] were symmetrically attached to the back of the aeroshell at the top and bottom, as shown in Fig. 4, to observe the vibrations of the aeroshell membrane surface. The resonant frequency

FIG. 4. Piezoelectric film and pressure tubes.

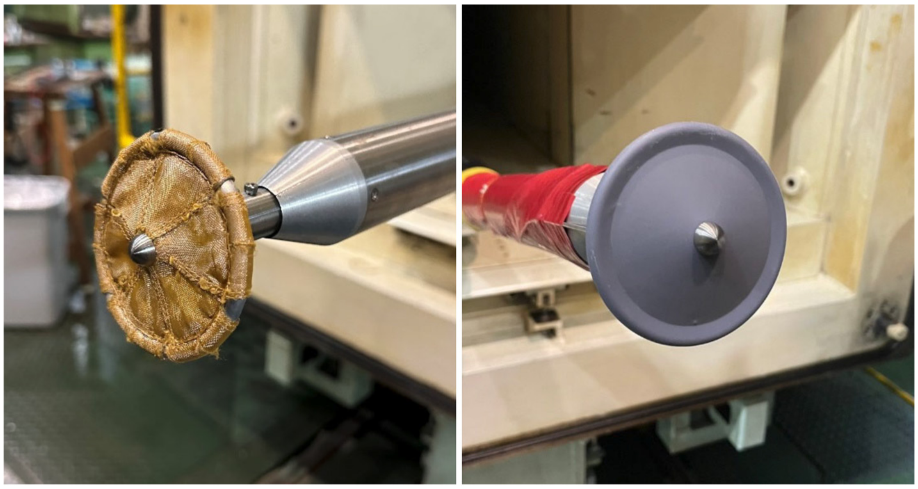

(a) Flexible aeroshell model (b) Rigid aeroshell model

FIG. 3. Experimental models.

of the piezoelectric film was 180 Hz, and it exhibited sufficient sensitivity in the frequency range of 10–300 Hz. In addition, a high-speed camera (Phantom Miro LC 311, Vision Research Ltd.)[28] was installed on the side of the model outside the windway to check the overall deformation behavior and deformational oscillation. The high-speed camera captured moving images at a frame rate of 2000 fps, a resolution of 1024×768, and an exposure time of 4.9×10^{-4} s.

D. Test conditions

Wind tunnel experiments were conducted at a freestream Mach number of 0.3, a freestream static pressure of 140 kPa, and a freestream temperature of 290 K. The wind tunnel flow was operated for 30 s, and measurements with a high-speed camera and piezoelectric film were taken 20 s after the start of wind tunnel operation. Measurements with the pressure tube were performed at four positions: 46 mm behind the capsule head, 24 mm from the center of the axis, and rotated 90°.

The angle of attack was varied for both the flexible aeroshell and rigid aeroshell models, and the tests were conducted at angles of attack of 0°, 5°, 10°, 15°, 20°, 30°, and 40°. Here, the angle of attack is defined as positive for pitch-up rotation about the z-axis. The straight sting was used for angles of attack of 0°–15°, and the 25° bent sting was used for angles of attack of 20°–40°, as shown in Figs. 5(a) and 5(b), respectively.

III. FSI ANALYSIS

The partitioned-coupled solution method was adopted for the FSI analysis in this study. The flow and structure fields were solved independently by different solvers, and data communication was performed at the coupling interface to establish the coupling of the fluid and structure. This partitioned approach has the advantage that sophisticated solvers can be employed for each type of analysis. Since accurately capturing the unsteady behavior of the flexible aeroshell's FSI response is essential, two-way coupling between the fluid and structural fields was performed within each time step. In addition to FSI, this partitioned two-way coupling approach is also employed in two-phase flow problems such as cavity capture,[29] demonstrating its versatility for application to various coupled problems.

In this study, the multi-physics simulation solver SU2[30] was used for the flow field simulations, and the nonlinear finite-element method solver CalculiX[31] was used for the structural simulations. In addition, the preCICE coupling library[32] was used to connect the solvers.

A. Coupling method

The aerodynamic forces obtained by the fluid solver and the deformation displacements obtained by the structure solver were exchanged in a two-way manner using the coupling library at the coupled interface. An implicit coupling scheme was used to exchange aerodynamic forces and displacements at the interface at each coupling time within a single time step to satisfy continuity and equilibrium conditions, as shown in Fig. 6. A quasi-Newton acceleration scheme[33] was used to improve the convergence efficiency and stability of the

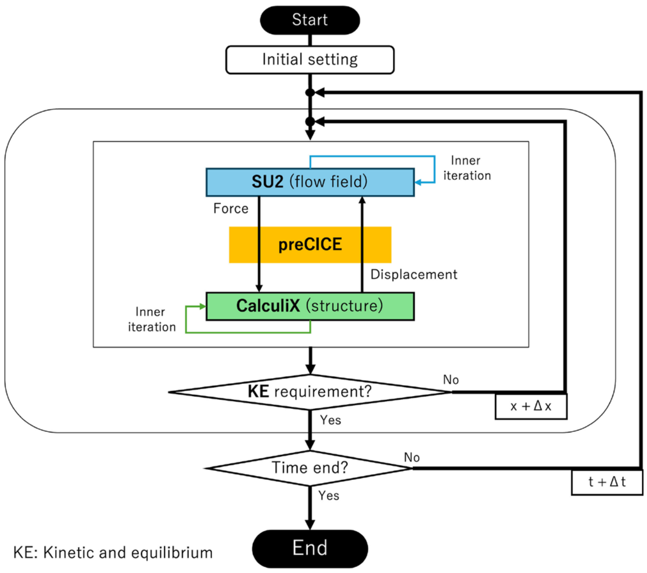

FIG. 6. Coupling flow chart.

(a) Straight sting (b) Bent sting

FIG. 5. Stings used in the present wind tunnel tests.

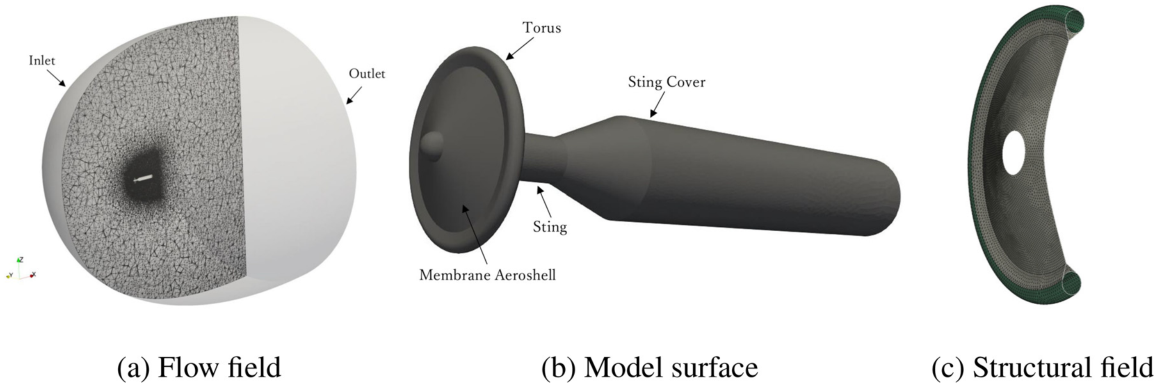

FIG. 7. Computational domains and grids.

coupled analysis. This method stabilizes and accelerates the coupling process based on a linear combination of previous iterations. Data exchange between solvers occurred at corresponding nodes on the coupled interface. The nearest-neighbor method was used for data mapping, because the flow and structural grids were not identical in this analysis.

B. Flow field model

The governing equations for the flow field are the compressible Navier–Stokes equations, which include the mass, momentum, and energy conservation laws. The gas was modeled as standard air, and its viscosity was evaluated using Sutherland's formula. Thermal conductivity was calculated using the viscosity, specific heat at constant pressure, and Prandtl number of 0.72. The version of SU2 was v-7.5.0 (Blackbird). The spatial gradient was calculated using the Green–Gauss method, and the advection term flux in the governing equation was computed using the Jameson–Schmidt–Turkel (JST) scheme with the sensor coefficients of 0.5 and 0.02 for the second and fourth orders, respectively. The viscous term flux was evaluated as the average of spatial gradients. Time integration was performed using the second-order dual-time stepping method. The coefficient matrix that appears in the internal iteration was solved using the flexible generalized minimal residual method (FGMRES), incorporating the upper-lower symmetric-Gauss–Seidel (LUSGS) method as a precondition. For parallel computation, SU2 decomposed the computational domain and managed the data communication across overlapping regions, using ParMETIS and message passing interface (MPI).

C. Structural field model

When subjected to aerodynamic forces, the shape of a flexible aeroshell differs significantly from its undeformed configuration. Therefore, an accurate structural model is essential for evaluating the coupled behavior between flexible structures and fluid flows. In this study, the finite-element analysis software CalculiX-v2.20 was used as the structural solver. In CalculiX, the triangular 3-node shell element was expanded to a 15-node wedge element. The use of shell elements reduces the number of structural mesh elements required. The governing equations of the structural mechanics are based on the principle of virtual work. The finite-element structural analysis requires solving the overall stiffness matrix, which is solved using the α-method,[34] where α is set to $-1/3$. The analysis was conducted in geometrically nonlinear mode to express large deformations. Calculations were performed in parallel using OpenMP.

D. Computational conditions

In this study, the computational domain for the fluid analysis was set to a hemispherical shape, as shown in Fig. 7(a), and the aeroshell to be analyzed was placed at the center. The computational domain was a coordinate system with an origin at the capsule head. The number of computational grids in this domain was approximately 7 500 000, all of which consisted of tetrahedral elements. The target of the analysis was a wind tunnel model that included a sting, as shown in Fig. 7(b). The computational grid for the structural side is illustrated in Fig. 7(c), where a portion of the mesh was cut away to show the cross section. The number of computational nodes is approximately 29 000. The coupled interfaces consisted of all computational grids in the structure domain and the surface of the aeroshell in the flow field domain. The joint between the thin aeroshell and capsule was fully constrained. In addition, the aeroshell and sting surfaces were subjected to no-slip boundary conditions and the wall surface temperature was set to 290 K.

A freestream boundary condition was set at the outer boundary of the fluid calculation domain, yielding a Mach number of 0.3, a static pressure of 140 kPa, and a temperature of 290 K. When the representative length is 0.08 m of the aeroshell diameter, the freestream flow Reynolds number is 7.66×10^5. The angle of attack was varied as 0°, 5°, 10°, 15°, and 30°. The time step of the fluid analysis was set to 1.25×10^{-5} s. In the calculation of aerodynamic coefficients, only aerodynamic forces excluding the balance cover were used, as in the wind tunnel test, with a characteristic length of 0.08 m and a characteristic area of 0.005 027 m^2. The center of the moment was located 29.8% of the aeroshell diameter from the capsule head.

The material properties of the structure differ between the thin aeroshell and torus sections. The torus had a density of 6000 kg/m^3 and a tube diameter of 0.75 mm to match the actual model and torus mass. Because the torus of the experimental model was made of aluminum and experienced minimal deformation, the Young's modulus and

Poisson's ratio were set to 70 GPa and 0.3, respectively. The aeroshell was made of Zylon fabric, and it was difficult to accurately evaluate the material properties while keeping computational simplicity to reduce computational cost. Therefore, in this study, an effective Young's modulus of 500 MPa was adopted as a linear material property, which was consistent with the results of the FSI analysis and experiments. This value is validated later through comparison with experimental data. The density and thickness were set to 900 kg/m^3 and 0.15 mm, respectively, which are the same as those of the Zylon fabrics used in actual models, and the Poisson's ratio was set to 0.3.

In addition, a computational fluid dynamics (CFD) analysis of the flow field was performed without considering structural deformation. This analysis was conducted using the same conditions and grid as those used in the FSI analysis.

E. Grid and timestep dependencies

To investigate the grid dependence of the fluid solver, the drag coefficients were compared by varying the number of grids in the computational domain of the fluid at a Mach number of 0.3 and an angle of attack of 0°. In this case, the computational mesh was uniformly refined throughout the domain. Figure 8 shows a comparison of the time-averaged drag coefficient for grid numbers ranging from 4 500 000 to 55 000 000. Convergence of the drag coefficient was observed, starting at a grid number of 7 500 000. The maximum difference between the largest and smallest grid cases was approximately 7.4%. Since the difference between the grid case with 7 500 000 cells, where the drag coefficient convergence begins, and the case with 55 000 000 cells was only about 2.2%, the number of computational grids for the fluid was set to 7 500 000.

Time step convergence was also confirmed. To evaluate the effect of time step size, we investigated whether there were any changes in the deformation behavior or aerodynamic coefficients by reducing the time step in the FSI analysis. Comparisons were made for time steps of 2.00×10^{-5}, 1.25×10^{-5}, and 5.00×10^{-6} s. The maximum displacement of the torus, deformation frequency, and the drag coefficient at each time step are presented in Table I. The differences in the maximum torus displacement and deformation frequency between 1.25×10^{-5} and 5.00×10^{-6} s were approximately 3.3% and 5.7%, respectively. The difference in the time-averaged drag coefficient was approximately 0.2%. A time step of 1.25×10^{-5} s was selected for this study to balance computational cost and accuracy.

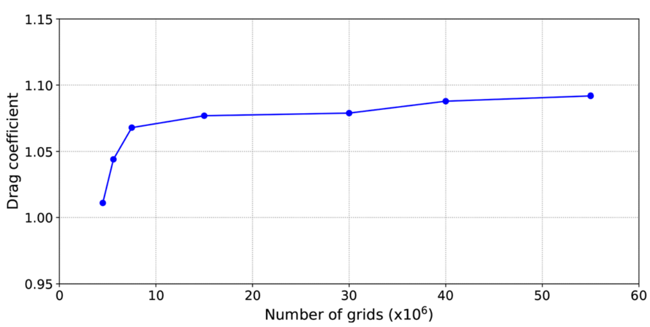

FIG. 8. Grid dependence of the flow field simulation.

TABLE I. Timestep dependence of the FSI simulation.

Time step (s)	Maximum displacement (mm)	Swing motion frequency (Hz)	Drag coefficient
2.00×10^{-5}	1.63	45.89	1.024
1.25×10^{-5}	1.51	43.32	1.028
5.00×10^{-6}	1.46	43.57	1.026

IV. RESULTS AND DISCUSSION

A. Eigenmodes

Insight into the free oscillations of vehicles is crucial for their design, as these oscillations reflect the dynamic characteristics of the vehicle, which depend solely on its material properties and geometry. The main objective of the free oscillation analysis is to prevent the negative effects of structural resonance on aerodynamics. This occurs when the natural frequency range of the structure overlaps with that of the aerodynamic loads. Such resonance generates high stresses, potentially leading to structural damage or unwanted deformation of the aeroshell. In addition, in FSI analysis, natural oscillations are also important for understanding the fundamental deformation modes of the structure. The natural oscillations of a flexible aeroshell were investigated using the finite-element solver CalculiX.

The eigenmodes and their corresponding eigenfrequencies (f) are shown in Fig. 9. The first and second modes (30.0 Hz) are pitching modes. These exhibit oscillation about the central axis with a 90° phase difference, which is a result of the symmetric geometry. The third mode (106.4 Hz) corresponds to rotational deformation in the roll direction about the body axis, exhibiting torsional behavior about the principal axis. The fourth mode (192.6 Hz) represents translational deformation of the torus along the body axis, resembling rigid-body motion along the axis. The fifth and sixth modes (472.8 Hz) are lateral motions centered at the torus, representing a lateral mode with a 90° phase difference. Modes from the seventh and above (695.5 Hz and higher) are localized deformations limited to the membrane surface, indicating higher-order surface vibrations. No other mode deformations involving components other than the membrane were observed.

B. Displacement mode in wind tunnel tests

The high-speed camera video captured during flow showed that the flexible aeroshell model oscillated (with a precessional motion) with a combination of the first and second eigenmodes. To capture this motion quantitatively, the motion of the torus was tracked using video. Figures 10(a) and 10(b) show the results of tracking the torus of the flexible aeroshell model from the high-speed camera at an angle of attack of 0° and its FFT analysis, respectively. One pixel in the video corresponded to approximately 0.185 mm, and the pitching deformation amplitudes were found to vary in the 0.4–1.3 mm range. The results of the FFT analysis also confirmed a peak at 42.5 Hz. Similarly, the results of the piezoelectric film attached to the back of the flexible model in the 0° angle of attack case and its FFT analysis are shown in Figs. 11(a) and 11(b), respectively. The vibration at 50 Hz is due to noise in the power line and is not important for evaluating the deformation behavior. A peak is observed at approximately 42.0 Hz,

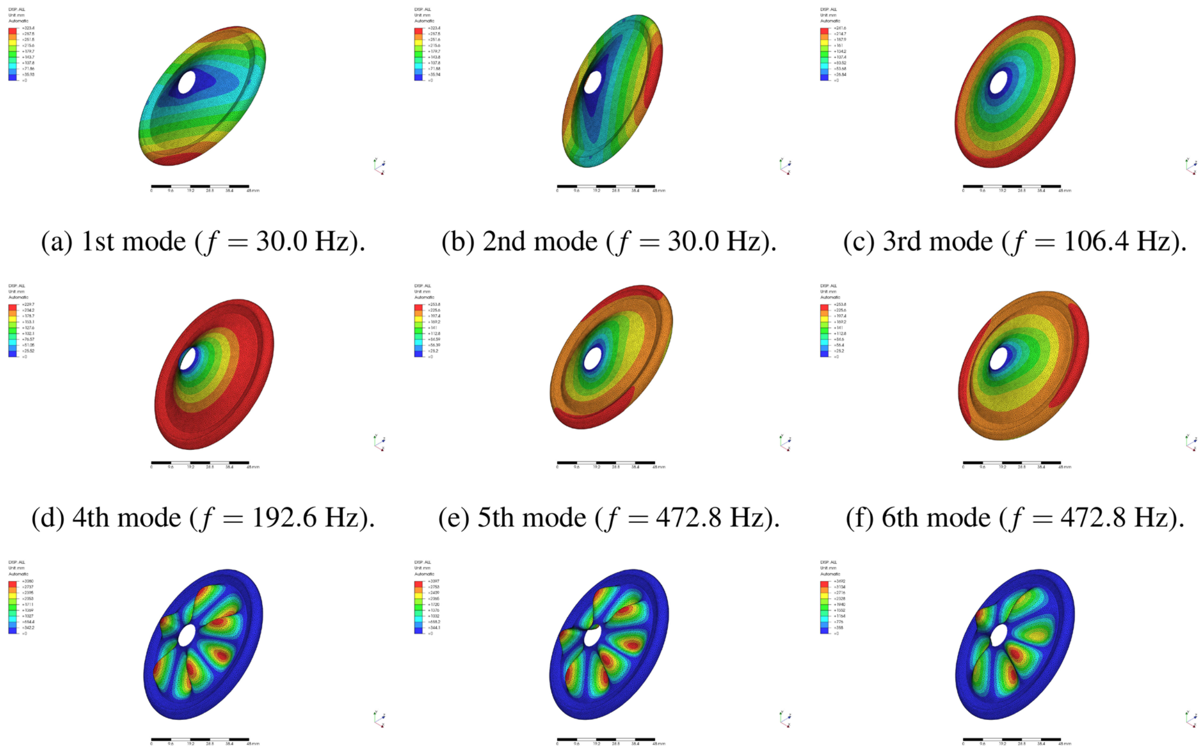

(a) 1st mode ($f = 30.0$ Hz). (b) 2nd mode ($f = 30.0$ Hz). (c) 3rd mode ($f = 106.4$ Hz).

(d) 4th mode ($f = 192.6$ Hz). (e) 5th mode ($f = 472.8$ Hz). (f) 6th mode ($f = 472.8$ Hz).

(g) 7th mode ($f = 695.5$ Hz) (h) 8th mode ($f = 695.9$ Hz) (i) 9th mode ($f = 730.3$ Hz)

FIG. 9. Eigenmode and corresponding eigenfrequency.

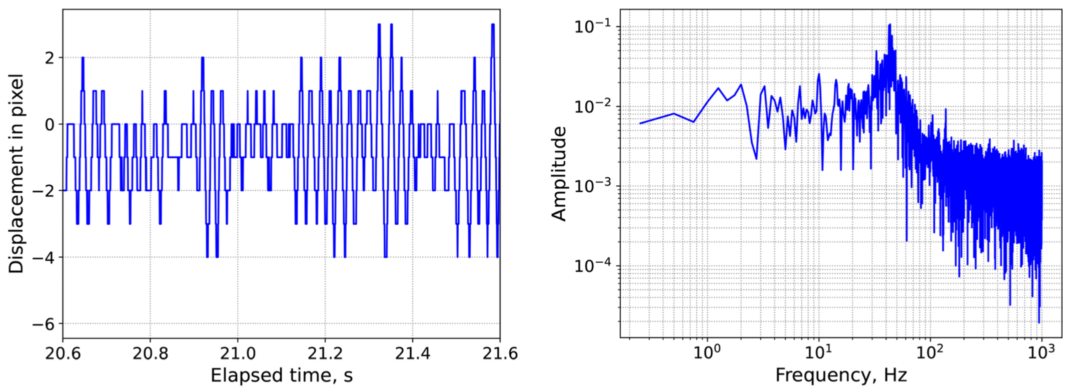

(a) History (b) FFT results

FIG. 10. Time history of torus displacement (in pixels) for the flexible aeroshell at an angle of attack of 0°, obtained using a tracking approach with a high-speed camera in the wind tunnel experiment.

indicating that the flexible model oscillated at a frequency of approximately 42.5 Hz.

In the case of the angle of attack, a similar swing deformation was observed, and the eigenfrequency of the oscillation remained almost unchanged regardless of the angle of attack.

C. Aeroshell deformation in FSI simulation

In the FSI analysis, the torus oscillated in the combined first and second eigenmodes, similar to the wind tunnel test. To understand the three-dimensional behavior of the aeroshell, the deformation behavior of the torus was investigated by plotting its direction vectors on a

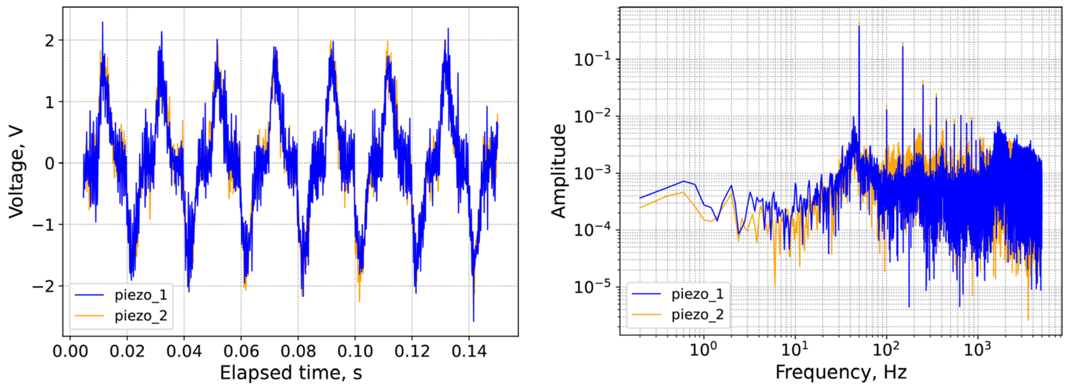

(a) History (b) FFT results

FIG. 11. Time history of voltage for the flexible aeroshell at an angle of attack of 0°, obtained from the piezoelectric film in the wind tunnel experiment.

virtual sphere, as shown in Fig. 12(a). The trajectories of the torus-direction vectors for the angles of attack of 0° and 15° are shown in Figs. 12(b) and 12(c), respectively. The plots were viewed from the front of the axis, with colors indicating the time normalized by the maximum computation time (0.346 s for an AOA of 0° and 0.225 s for an AOA of 15°). The center of the circle is a point on the axis of the model, and each circle represents the tilt of the direction vector of the torus relative to the body axis. Aerodynamic loads deform the aeroshell, causing it to undergo precessional motion.

The aeroshell's membrane is composed of Zylon fabric, which typically does not exhibit simple linear material behavior. Therefore, it is necessary to identify an effective Young's modulus that can reproduce the aeroshell behavior observed in wind tunnel experiments using FSI analysis. The effective Young's modulus was identified by comparing the results of the wind tunnel tests with those of the FSI analysis for a 0° angle of attack. The FSI analysis showed the same swing deformation (combined mode of the first and second modes) as that in the wind tunnel tests. This swing deformation occurred in various directions, and the combined modes caused the torus displacement to appear as if it were moving in the rolling direction. Table II presents a comparison of the frequencies of the swing and natural oscillations for each Young's modulus in the FSI analysis. Here, the natural oscillation frequencies are the frequencies of the first eigenmodes. The swing oscillation in the FSI analysis was higher than that of the natural oscillation. In general, the FSI oscillation modes and natural frequencies of a flexible structure placed in a fluid do not coincide. This has also been demonstrated through displacement analysis of flexible structures using dynamic mode decomposition.[23,24] Therefore, it was reasonable to validate the results through comparison with the experimental data. A Young's modulus of 500 MPa was adopted as the effective value because the frequency of the swing oscillation in the FSI analysis was closest to that in the wind tunnel test (42.5 Hz).

The Young's modulus of the Zylon filaments (fiber alone) was 180 GPa; however, the effective Young's modulus significantly decreased when the fiber was woven into the fabric. Aeroshells are fabricated by sewing Zylon fabrics together, and the effects of seams created during this process cannot be ignored. Therefore, it is difficult to calculate the effective value based on catalog values. Yamada *et al.*[35] conducted wind tunnel tests and coupled fluid–structure analyses of a flexible structural aeroshell at hypersonic speeds. They estimated the effective Young's modulus by matching the torus displacement, obtaining a value of approximately 1.0 GPa. Therefore, an effective Young's modulus of 500 MPa in the present study is reasonable in comparison with the previous result.

The displacement history of the torus and the FFT results for the flexible aeroshell are shown in Figs. 13(a) and 13(b), respectively, at an angle of attack of 0°. Although the amplitudes were slightly overestimated, the results generally agreed with those of the wind tunnel test.

The high-frequency displacement vibration that appeared early in the FSI analysis was the axial translational deformation of the torus, as indicated by the 4th eigenfrequency mode with a vibration frequency of approximately 190 Hz. This is because the 4th eigenmode appeared owing to the dynamic pressure at the beginning of aeroshell deformation. This vibration, induced by structural deformation, is progressively damped over time due to energy dissipation resulting from aerodynamic forces. In addition, aeroshell surface deformation, which was a combination of the seventh and higher deformation modes, was observed.

The average torus angles with respect to the angle of attack are shown in Fig. 14. In both the wind tunnel tests and FSI analysis, the torus angle increased as the angle of attack increased, as listed in Table III. This tilt of the torus perpendicular to the flow is attributed to structural deformation of the aeroshell caused by differences in dynamic pressure between its top and bottom surfaces. In the wind tunnel tests, the torus translated, rotated, and oscillated nearly perpendicular to the flow up to an angle of attack of approximately 10°. In contrast, the torus deformation observed in the FSI analysis was smaller, and the torus angle varied linearly with the angle of attack. This difference may be due to the use of linear material properties and the inclusion of repulsive forces from compression in the structural model used for the FSI analysis. Another reason may be the difficulty in modeling the joint between the aeroshell and the capsule section.

In this study, the effective Young's modulus was determined to match the frequencies of the swinging modes. This modulus provides good agreement for displacement modes primarily caused by tension, such as the swinging modes (1st and 2nd eigenmodes) and the translational displacement in the freestream direction (4th eigenmode).

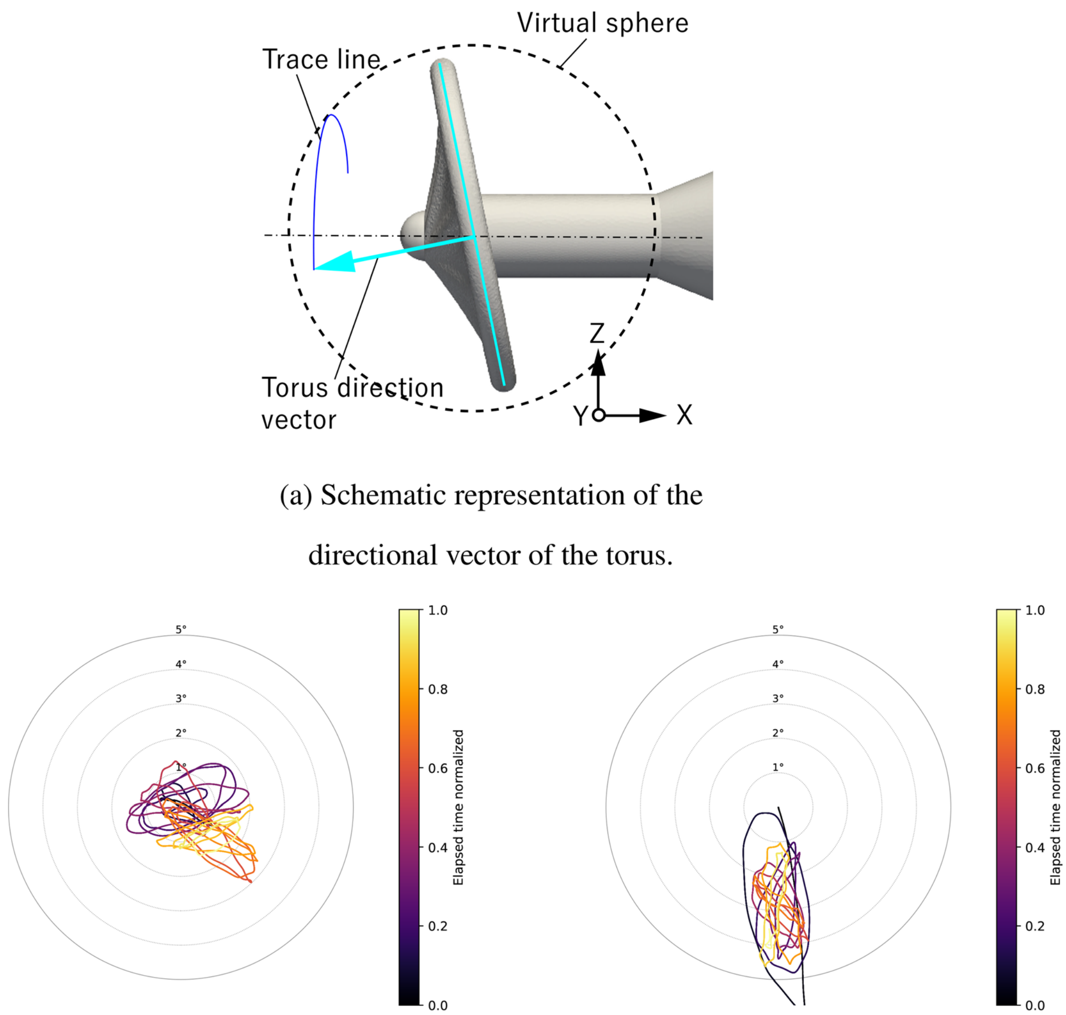

(a) Schematic representation of the directional vector of the torus.

(b) AOA 0 degrees

(c) AOA 15 degrees

FIG. 12. Trajectory of the torus-direction vector. The plot colors indicate time normalized by the maximum computation time (0.346 s for an angle of attack of 0° and 0.225 s for 15°).

TABLE II. Frequency comparison of swing oscillations between the eigenmode and FSI simulation for different Young's moduli.

Young's modulus (MPa)	300	400	500	700
Eigenmode (Hz)	23.4	27.0	30.0	35.7
FSI analysis (Hz)	33–36	37–42	41–47	50–53

However, it may not accurately predict modes involving bending deformation, such as membrane surface deformation (7th eigenmode). Additionally, it is difficult to model the seams and the connection to the capsule section accurately. Therefore, the limitations of this analysis model include potential inaccuracies in predicting such displacement modes.

D. Aerodynamic characteristics

1. Case without angle of attack

The forces acting along the x, y, and z axes are defined as the drag, side, and lift forces, respectively. The moments acting around the x, y, and z axes are defined as the rolling, pitching, and yawing moments, respectively. The aerodynamic coefficient histories of the flexible and rigid aeroshells for an angle of attack of 0° in the wind tunnel tests are shown in Fig. 15. Each aerodynamic coefficient is a non-dimensional version of the forces and moments measured by a six-component force balance. In the aerodynamic history of the flexible model, the time averages of pitching moment, yawing moment, side force, and lift force coefficients were not zero. This was attributed to the asymmetry of the model caused by the piezoelectric film attached to the back of the model.

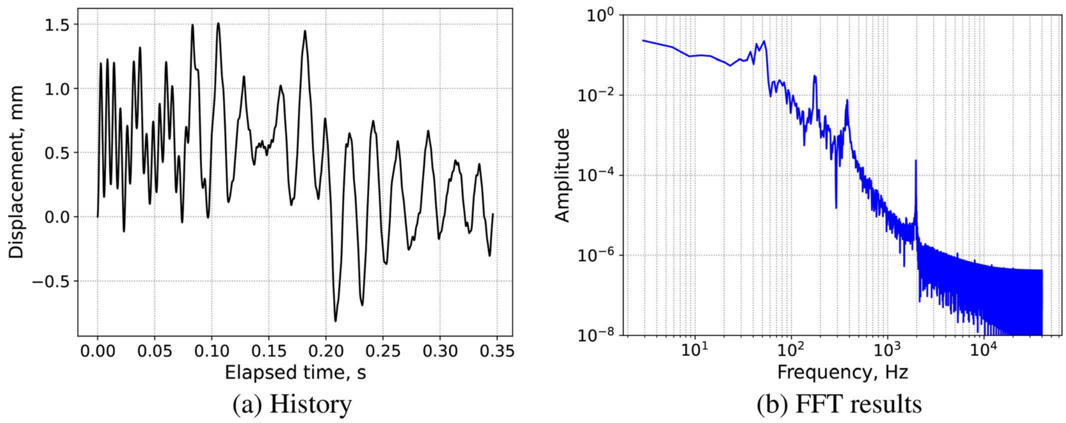

FIG. 13. Time history of torus displacement for the flexible aeroshell at an angle of attack of 0°, obtained from numerical simulation.

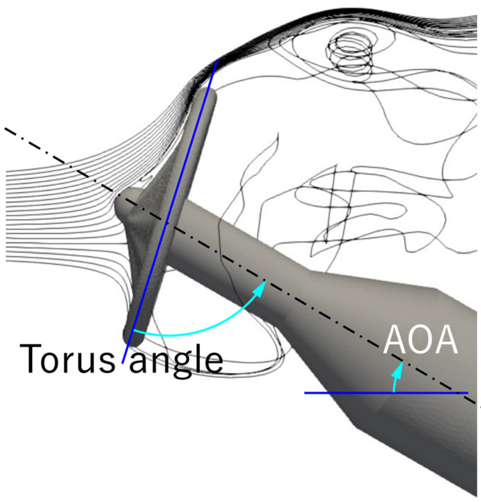

FIG. 14. Schematic of torus angle.

TABLE III. Averaged torus angle.

Angle of attack (deg)	0	5	10	15	20	30
Experiment (deg)	89	84	81	79	78	75
FSI simulation (deg)	90	89	88	87	⋯	84

Figures 16(a) and 16(b) show the FFT analysis results for drag force and pitching moment coefficients of the flexible and rigid aeroshells obtained from the wind tunnel tests, respectively. In the FFT analysis results of pitching moment, the peaks at approximately 65, 137, and 224 Hz were commonly observed in both the flexible and rigid aeroshells due to sting and aerodynamic vibrations. In contrast, a peak at approximately 42 Hz was observed only in the flexible model. This is consistent with the frequency of the swing oscillation in the model. In addition, the FFT analysis of drag force showed a peak unique to the flexible aeroshell at approximately 84 Hz, which is twice the frequency of the pitching moment. This indicates that the swing oscillation also affects the aerodynamic coefficients of the aeroshell.

2. Case with angle of attack

The histories of aerodynamic coefficients and torus angle from the FSI analysis of the flexible aeroshell at an angle of attack of 15° are shown in Fig. 17. In addition, Fig. 18 shows the aerodynamic coefficient histories from the CFD analysis for the rigid aeroshell under the same angle of attack. The FSI analysis revealed that the lift coefficients and pitching moment varied with changes in the torus angle. The torus translated and rotated in directions perpendicular to the flow due to the aeroshell deformation. In this case, the pitching moment shifted toward the positive direction as the torus tilted vertically, implying that the torus became oriented perpendicular to the flow, which may lead to aerodynamic instability. In contrast, in the CFD analysis of the rigid aeroshell, the pitching moment coefficient remained consistently negative, indicating that the aerodynamic forces acted to stabilize the model's attitude. These results indicate that, compared to a rigid aeroshell, a flexible aeroshell is more susceptible to attitude instability at Mach 0.3, which lies within the subsonic speed regime.

The time-averaged aerodynamic coefficients were compared for each angle of attack. Figure 19(a) shows the time-averaged drag, lift, and side force coefficients for the wind tunnel experiments and numerical simulations of flexible and rigid aeroshells. In both the wind tunnel experiments and simulations, the lift force tended to become more negative as the angle of attack increased. This behavior for the flexible aeroshell differed between the wind tunnel tests and numerical simulations, which was attributed to the differences in the torus angle, with slightly larger lift values observed in the wind tunnel test due to a larger torus angle. In contrast, the rigid aeroshell showed good agreement in the lift results. The lift force exhibited a weaker negative trend at higher angles of attack, particularly in the flexible aeroshell model. This suggests that the z-directional force on the model was weakened when the torus was tilted perpendicular to the flow. This suggests that the z-directional force on the model was weakened when the torus was tilted perpendicular to the flow.

Figure 19(b) compares the time-averaged pitching, yawing, and rolling moment coefficients for each angle of attack in the numerical

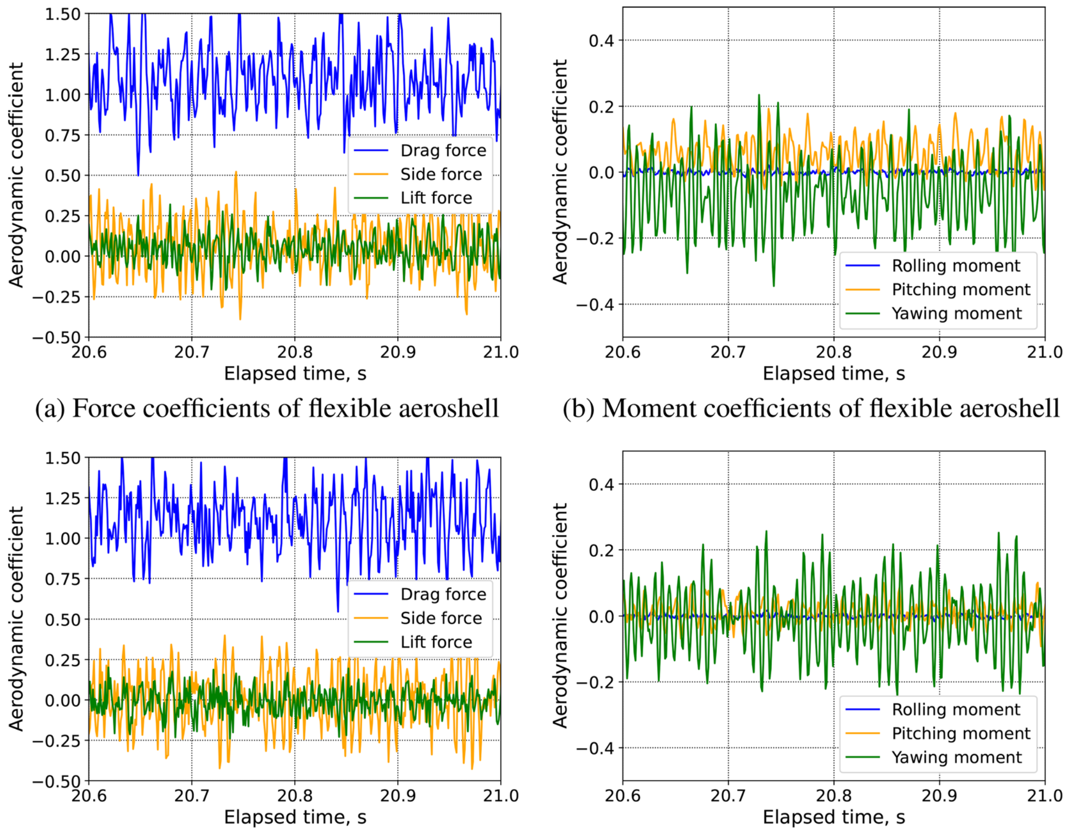

(a) Force coefficients of flexible aeroshell (b) Moment coefficients of flexible aeroshell

(c) Force coefficients of rigid aeroshell (d) Moment coefficients of rigid aeroshell

FIG. 15. Time histories of aerodynamic force and moment coefficients at an angle of attack of 0°, obtained from wind tunnel tests.

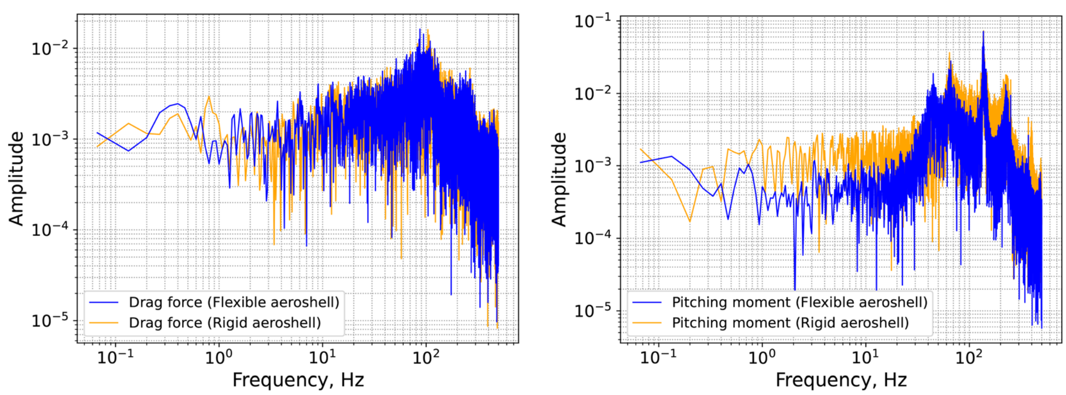

(a) Drag force coefficient (b) Pitching moment coefficient

FIG. 16. Comparisons of FFT analysis results for flexible and rigid aeroshells at an angle of attack of 0°, obtained from wind tunnel tests.

simulations of the flexible and rigid aeroshells. In both cases, pitching moment tended to become more negative with increasing angle of attack. This indicates that the aerodynamic force responsible for attitude stabilization is induced by the inclination of the model. However, in the flexible aeroshell simulation, the pitching moment shifted toward the positive direction relative to the rigid case, suggesting that the deformation of the aeroshell weakened the aerodynamic characteristics responsible for maintaining attitude stability.

The aerodynamic forces acting on the wind tunnel model, particularly those that strongly influence attitude determination, are

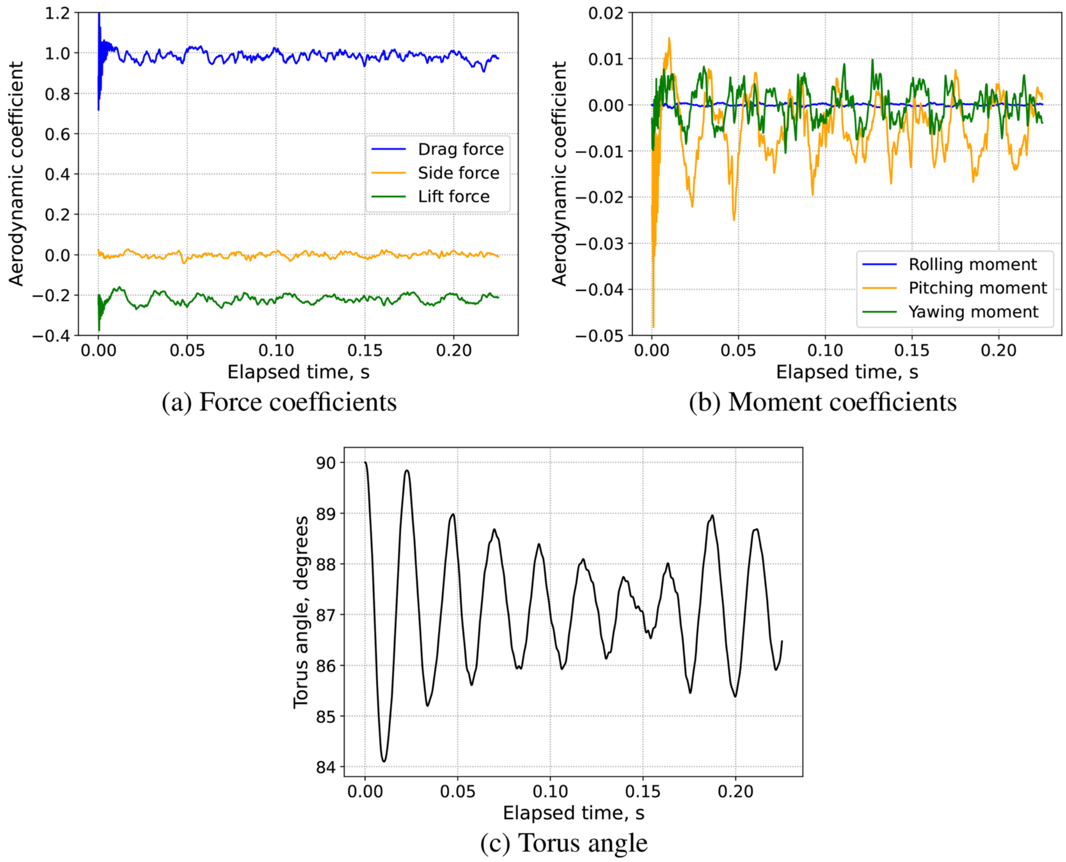

FIG. 17. Time histories of aerodynamic coefficients and torus angle for the flexible aeroshell at an angle of attack of 15°, obtained from numerical simulation.

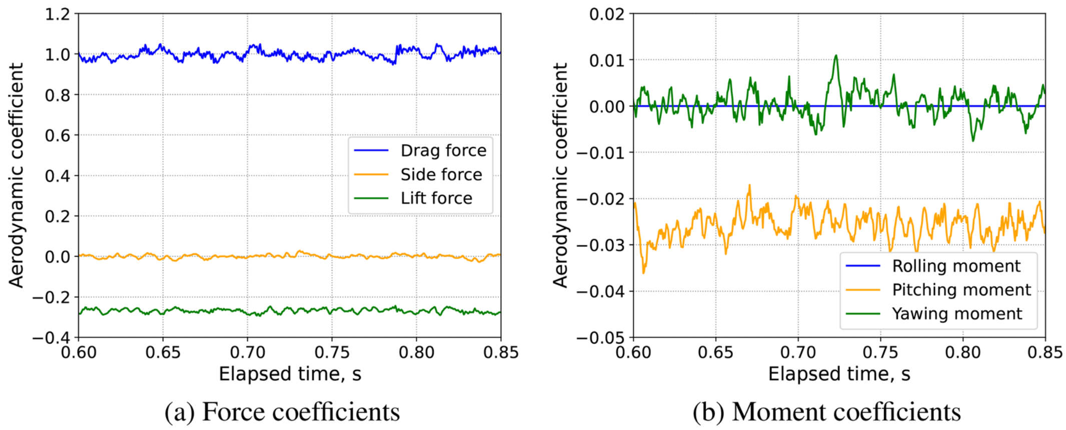

FIG. 18. Time histories of aerodynamic coefficients for the rigid aeroshell at an angle of attack of 15°, obtained from numerical simulation.

variables that are significantly affected by the modes induced by tensile forces. Therefore, we believe the reliability of the FSI model is crucial for their evaluation. On the contrary, high-frequency displacements associated with membrane surface deformation and their effects on aerodynamic forces are not necessarily captured accurately. However, these effects are not critical within the scope of the present study. Although the torus angle is not fully reproduced, the model still captures the trend of moment evaluation.

E. Flow field around flexible aeroshell

To investigate the effects of the attitude and deformation of the aeroshell on the flow field, a comparison was made for each angle of

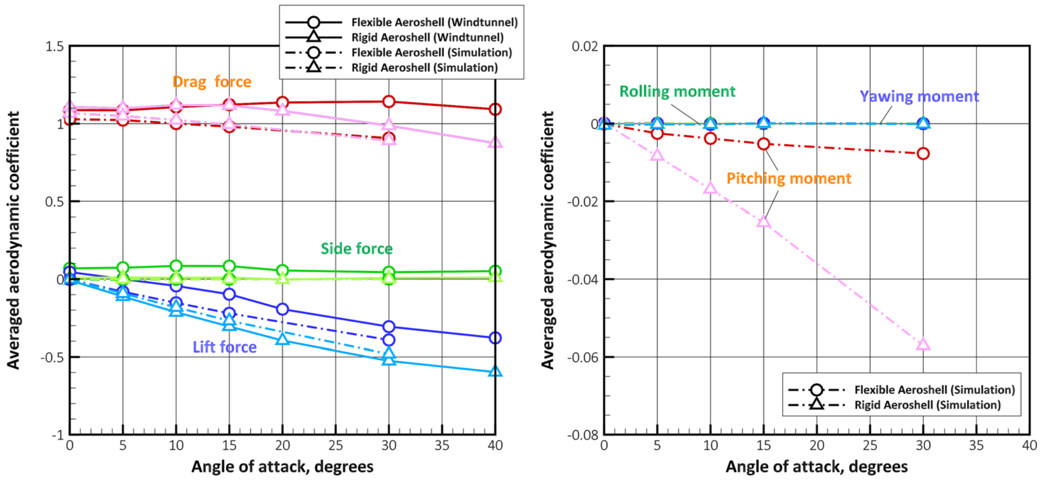

(a) Time-averaged aerodynamic force coefficients.

(b) Time-averaged aerodynamic moment coefficients.

FIG. 19. Comparison of time-averaged aerodynamic coefficients at each angle of attack between wind tunnel experiments and simulations for flexible and rigid aeroshells.

attack using the computed results from the FSI simulations. The instantaneous distributions of the Mach number, pressure coefficient, and the second invariant of the velocity gradient tensor (the Q criterion) around the flexible aeroshell at angles of attack of 0°, 15°, and 30° are shown in Figs. 20(a)–20(c), respectively. A large recirculation area was observed behind the aeroshell. In the shear layer, which is the boundary of the recirculation region, the difference in velocity causes the waves to grow and generates a low-pressure vortex. In this wake region, the Q criterion becomes high in all these cases, and the vortex structure is dominant. Oscillations with frequencies higher than the swinging motion observed in the pitching moment and drag force histories are considered to originate from the generation of these wake vortices. The freestream stagnates in front of the aeroshell, thereby creating a high-pressure region. In contrast, a low-pressure region was generated at the rear of the aeroshell. The pressure difference between the high-pressure front and the low-pressure rear causes significant aerodynamic drag, enabling the flexible aeroshell to function as an efficient aerodynamic decelerator. The high-pressure region created in front of the aeroshell shifts toward the windward side of the aeroshell as the angle of attack increases. This change in the pressure distribution in front of the aeroshell induces a pitching moment shift toward the positive direction, resulting in attitude instability.

Although the simulation results of the rigid aeroshell model are not shown here, the fundamental structures of the near-field flow were almost identical between the rigid and flexible models. Specifically, the flow stagnates at the front of the model, forming a high-pressure region, while flow separation occurs at the torus section, generating a low-pressure wake and recirculation region behind the model. However, in the flexible model, deformation of the aeroshell and the displacement of the torus alter the surface pressure distribution, significantly affecting the aerodynamic forces, particularly the pitching moment. Minor differences in the separation points near the capsule head and the top of the torus were observed, but their impact on the overall aerodynamic forces was low. Similar to the wind tunnel test, the flexible model simulation also revealed aerodynamic oscillations corresponding to the pitch vibration frequencies. In addition, a characteristic 84 Hz oscillation, associated with the swinging motion, was clearly observed in the drag coefficient.

V. CONCLUSIONS

In this study, wind tunnel experiments were conducted using flexible and rigid aeroshells at subsonic speeds in a wind tunnel. The attitude characteristics and aerodynamic effects of the aeroshell deformation were evaluated by conducting tests at various angles of attack. A coupled fluid–structure interaction (FSI) analysis was also performed using open-source software with a partitioned coupling approach under the same conditions as the wind tunnel experiment. In this FSI analysis, SU2 was used as the fluid solver, and CalculiX was used as the structure solver, coupled via preCICE, a coupling library. A geometrically nonlinear and materially linear model was employed for the structural analysis. By comparing the results of these analyses, the static attitude characteristics of the flexible aeroshell and its coupled behavior were evaluated. In addition, the FSI analysis model was validated by comparing the wind tunnel experiments. The fluid–structure interaction effects were also clarified through comparisons between the flexible and rigid models.

It was confirmed that the flexible aeroshells induced swing oscillations because of their deformation. The effective Young's modulus was determined by identifying that of the aeroshell's membrane at which the frequency of the swing oscillation matched that observed in the FSI analysis and wind tunnel experiment. The swing deformation of the aeroshell is reflected in the aerodynamic characteristics, demonstrating that the deformation affects the aerodynamic coefficients. The swing oscillation was not affected by the angle of attack, and the oscillation frequency changed only slightly. The deformation

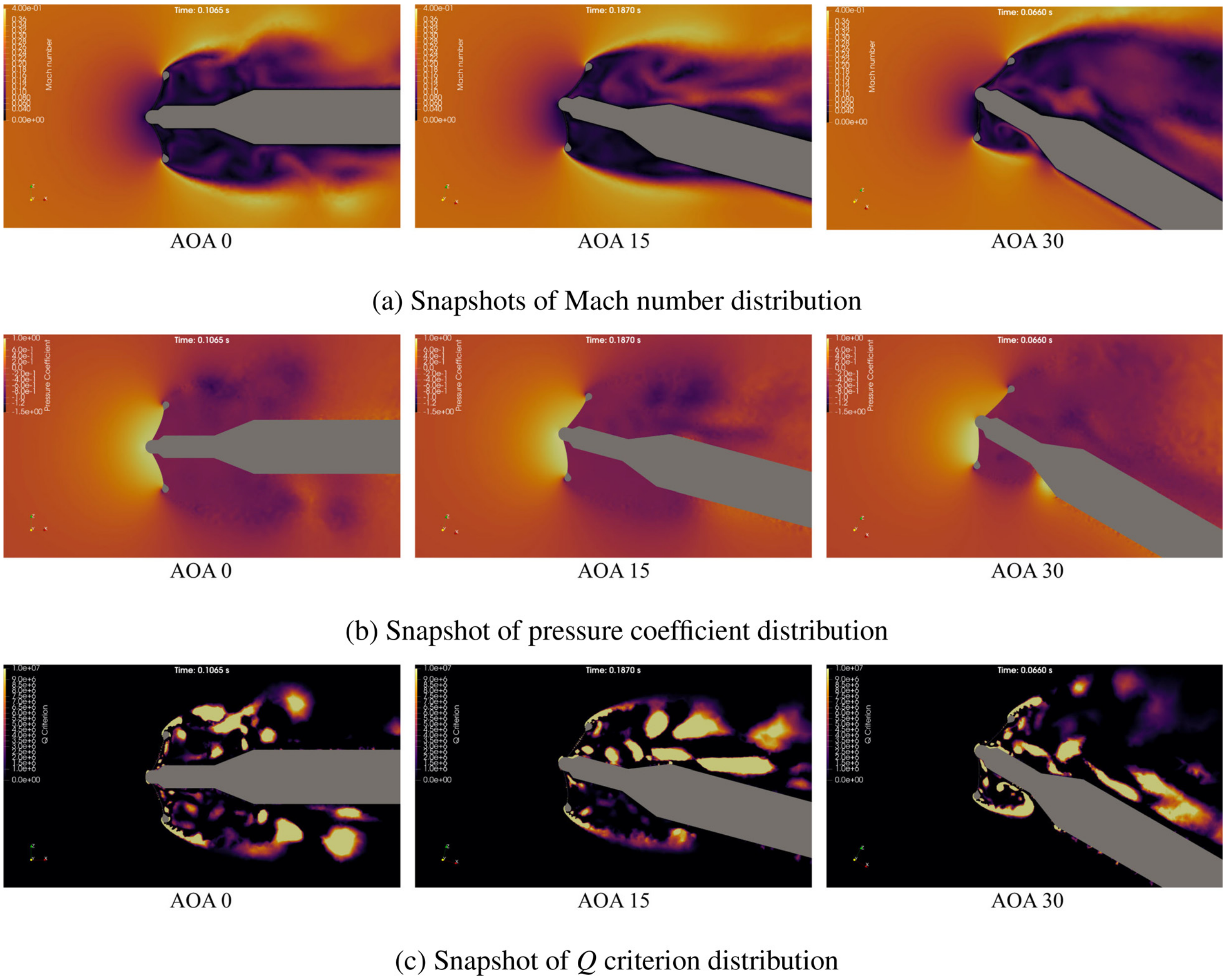

FIG. 20. Flow fields around the flexible aeroshell at three angles of attack, obtained from numerical simulations.

behavior of the flexible aeroshell was consistent with the aerodynamic behavior observed in both the wind tunnel experiment and FSI analysis.

As the angle of attack increased, the pitching moment became more negative for the rigid aeroshell, and the attitude characteristics became more stable. Conversely, the flexible aeroshell exhibited a shift in the pitching moment toward the positive direction due to the aerodynamic deformation of the entire structure. This shift reduced its static attitude stability compared to the rigid aeroshell, making it more susceptible to instability.

A linear material model was used for the structural analysis in this computational model. While this approach contributes to the simplification of the computational model, it requires the identification of an effective Young's modulus through comparison with experimental results. However, since the predicted deformation modes under tensile loading are consistent with the observed behavior, it is unlikely that this simplification will significantly affect the accuracy of aerodynamic behavior predictions. However, proper modeling of seams and joints with the capsule, as well as accurate prediction of membrane surface deformation, requires further validation. Improving the accuracy of displacement prediction through these aspects remains a subject for future work.

This study demonstrated that the static attitude stability of a flexible aeroshell decreases when the structure deforms under aerodynamic forces. Since attitude instability during actual flexible aeroshell operations, such as atmospheric entry, can lead to significant changes in aerodynamic characteristics and degraded landing-site accuracy, it is crucial to develop design strategies to prevent such issues. From this perspective, the present FSI simulation model has proven effective, enabling the identification of initial aeroshell shapes that ensure the necessary attitude stability. Securing attitude stability remains a major concern for flexible aeroshell technologies. Since this study employed a subscale model at subsonic speeds for comparison with experimental results and model validation, updates to the analysis model will be necessary for full-scale applications and for transonic or higher-speed regimes.

ACKNOWLEDGMENTS

The authors sincerely thank Mr. Tadayuki Yoshio, Mr. Tomoki Sakai, and Mr. Kaito Wakabayashi, Hokkaido University, for incorporating the wind tunnel tests. This study was supported by the Japan Society for the Promotion of Science (JSPS) KAKENHI (Grant Nos. 23H00212 and 24K01072). The present computations used the computational resources of the SQUID provided by the Cybermedia Center, Osaka University, through the HPCI System Research Project (Project ID: hp240004). The wind tunnel experiments were conducted in the transonic wind tunnel of the Japan Aerospace Exploration Agency as an interuniversity research institute facility (Project ID: W23-001).

AUTHOR DECLARATIONS

Conflict of Interest

The authors have no conflicts to disclose.

Author Contributions

Yosuke Fujita: Conceptualization (equal); Data curation (equal); Formal analysis (equal); Investigation (equal); Methodology (equal); Software (equal); Validation (equal); Visualization (equal); Writing – original draft (equal). **Sanjoy Kumar Saha:** Conceptualization (supporting); Data curation (supporting); Formal analysis (supporting); Investigation (equal); Methodology (equal); Software (equal); Validation (lead); Visualization (equal); Writing – original draft (supporting); Writing – review & editing (supporting). **Yusuke Takahashi:** Conceptualization (lead); Funding acquisition (lead); Project administration (lead); Resources (lead); Software (lead); Supervision (lead); Validation (supporting); Writing – original draft (supporting); Writing – review & editing (lead). **Kazuhiko Yamada:** Conceptualization (equal); Data curation (supporting); Funding acquisition (equal); Project administration (lead); Resources (equal); Supervision (equal); Writing – review & editing (lead).

DATA AVAILABILITY

The data that support the findings of this study are available from the corresponding author upon reasonable request.

REFERENCES

[1]S. J. Hughes, R. A. Dillman, B. R. Starr, R. A. Stephan, M. C. Lindell, C. J. Player, and D. F. M. Cheatwood, "Inflatable re-entry vehicle experiment (IRVE) design overview," AIAA Paper No. 2005-1636, 2005.

[2]M. Lindell, S. Hughes, M. Dixon, and C. Willey, "Structural analysis and testing of the inflatable re-entry vehicle experiment (IRVE)," AIAA Paper No. 2006-1699, 2006.

[3]D. Litton, D. Bose, F. Cheatwood, S. Hughes, H. Wright, M. Lindell, S. Derry, and A. Olds, "Inflatable re-entry vehicle experiment (IRVE)-4 overview," AIAA Paper No. 2011-2580, 2011.

[4]S. J. Hughes, D. F. M. Cheatwood, A. M. Calomino, and H. S. Wright, "Hypersonic inflatable aerodynamic decelerator (HIAD) technology development overview," AIAA Paper No. 2011-2524, 2011.

[5]K. Yamada and K. Suzuki, "A particle-based model and its validation for deformation analysis of membrane aeroshell," J. Jpn. Soc. Aeronaut. Space Sci. **53**, 51–60 (2005).

[6]K. Yamada, Y. Nagata, T. Abe, K. Suzuki, O. Imamura, and D. Akita, "Suborbital reentry demonstration of inflatable flare-type thin-membrane aeroshell using a sounding rocket," J. Spacecr. Rockets **52**, 275–284 (2015).

[7]T. Nakao, K. Yamada, H. Hamori, T. Ishimaru, S. Imai, Y. Nagata, K. Maeda, K. Maehara, H. Habu, Y. Akimoto *et al.*, "Overview of reentry and recovery module with deployable aeroshell technology for sounding rocket experiment," AIAA Paper No. 2022-2710, 2022.

[8]K. Yamada, Y. Nagata, and T. Nakao, "Flight data analysis of reentry capsule with deployable aeroshell in sounding rocket S-520-31 experiment," AIAA Paper No. 2022-2712, 2022.

[9]Y. Takahashi, K. Yamada, T. Abe, and K. Suzuki, "Aerodynamic heating around flare-type membrane inflatable vehicle in suborbital reentry demonstration flight," J. Spacecr. Rockets **52**, 1530–1541 (2015).

[10]Y. Takahashi, D. Ha, N. Oshima, K. Yamada, T. Abe, and K. Suzuki, "Aerodecelerator performance of flare-type membrane inflatable vehicle in suborbital reentry," J. Spacecr. Rockets **54**, 993–1004 (2017).

[11]I. Clark, J. Cruz, M. Hughes, J. Ware, A. Madlangbayan, and R. Braun, "Aerodynamic and aeroelastic characteristics of a tension cone inflatable aerodynamic decelerator," AIAA Paper No. 2009-2967, 2009.

[12]R. Kramer, F. Cirak, and C. Pantano, "Fluid–structure interaction simulations of a tension-cone inflatable aerodynamic decelerator," AIAA J. **51**, 1640–1656 (2013).

[13]J. Wu, Z. Zhang, A. Hou, X. Xue, and X. Cao, "Thermal aeroelastic characteristics of inflatable reentry vehicle experiment (IRVE) in hypersonic flow," Int. J. Aerosp. Eng. **2021**, 673818.

[14]B. R. Hollis, "Surface heating and boundary-layer transition on a hypersonic inflatable aerodynamic decelerator," J. Spacecr. Rockets **55**, 856–876 (2018).

[15]Y. Takahashi, T. Koike, N. Oshima, and K. Yamada, "Aerothermodynamic analysis for deformed membrane of inflatable aeroshell in orbital reentry mission," Aerosp. Sci. Technol. **92**, 858–868 (2019).

[16]Y. Nagata, K. Yamada, T. Abe, and K. Suzuki, "Attitude dynamics for flare-type membrane aeroshell capsule in reentry flight experiment," AIAA Paper No. 2013-1285, 2013.

[17]K. Hiraki, "Experimental study on dynamic instability of capsule-shaped body," ISAS Report No. (The Institute of Space and Astronautical Science, 1999), pp. 1–55 (in Japanese).

[18]S. Koga, A. Hidaka, R. Tagai, T. Kimura, T. Yoshinaga, S. Nagai, and H. Nishijima, "Dynamic stability testing of a reentry lifting capsule in a transonic wind tunnel," AIAA Paper No. 2014-1119, 2014.

[19]H. Takasawa, T. Fujii, Y. Takahashi, T. Moriyoshi, H. Takayanagi, Y. Nagata, and K. Yamada, "Static attitude stability of deep space sample return capsule with thin aeroshell," CEAS Space J. **17**, 55–69 (2025).

[20]H. Takasawa, T. Fujii, K. Hirata, T. Moriyoshi, Y. Takahashi, Y. Nagata, and K. Yamada, "Dynamic instability modeling on phase plane for thin aeroshell capsule with pitching motion at transonic speed," Mech. Eng. J. **11**, 24-00053 (2024).

[21]S. K. Saha, J. Tobari, Y. Takahashi, N. Oshima, T. Moriyoshi, K. Yamada, and R. Shibata, "Fluid-structure interaction characteristics of inflatable reentry aeroshell at subsonic speed," Aerosp. Sci. Technol. **133**, 108112 (2023).

[22]S. K. Saha and Y. Takahashi, "Aerostructural analysis of a deployable aeroshell in transonic flow," AIAA J. **62**, 4589–4604 (2024).

[23]Y. Takahashi, "Spatiotemporal mode extraction for fluid–structure interaction using mode decomposition," J. Sound Vib. **597**, 118804 (2025).

[24]S. K. Saha and Y. Takahashi, "Mode decomposition to identify oscillation patterns of flexible aeroshell," Phys. Fluids **36**, 116108 (2024).

[25]I. Funaki, S. Nonaka, K. Yamada, and Y. Maru, "Overview of ISAS/JAXA wind tunnel facility," Aeronaut. Space Sci. Jpn. **64**, 199–208 (2016) (in Japanese).

[26]Toyobo Corporation, see http://www.toyobo-global.com/seihin/kc/pbo/ for "Zylon technical data."

[27]Parallax Inc., see https://www.parallax.com/package/piezo-film-vibra-tab-downloads/ for "Piezo film vibra tab downloads."

[28]Vision Research Ltd., see https://www.phantomhighspeed.com/-/media/project/ameteksxa/visionresearch/documents/manuals/mirolablcrmanual.pdf for "Phantom Miro LAB/LC/R series manual."

[29]Z. Wang, H. Cheng, X. Luo, X. Peng, and B. Ji, "An improved Eulerian–Lagrangian method combined with ductile material model for cavitation erosion assessment," J. Fluids Eng. **147**, 051502 (2025).

[30]T. D. Economon, F. Palacios, S. R. Copeland, T. W. Lukaczyk, and J. J. Alonso, "SU2: An open-source suite for multiphysics simulation and design," AIAA J. **54**, 828–846 (2016).
[31]G. Dhondt and K.Wittig, see https://www.calculix.de for "CalculiX – A free software three-dimensional structural finite element program."
[32]H.-J. Bungartz, F. Lindner, B. Gatzhammer, M. Mehl, K. Scheufele, A. Shukaev, and B. Uekermann, "preCICE–A fully parallel library for multi-physics surface coupling," Comput. Fluids **141**, 250–258 (2016).
[33]J. Degroote, P. Bruggeman, R. Haelterman, and J. Vierendeels, "Stability of a coupling technique for partitioned solvers in FSI applications," Comput. Struct. **86**, 2224–2234 (2008).
[34]I. Miranda, R. M. Ferencz, and T. J. R. Hughes, "An improved implicit-explicit time integration method for structural dynamics," Earthquake Eng. Struct. Dyn. **18**, 643–653 (1989).
[35]K. Yamada, Y. Kato, and T. Abe, "Numerical simulation of hypersonic flow around flare-type aeroshell with torus frame," in Proceedings of 6th Asia Workshop on Computational Fluid Dynamics, Kashiwa, Japan (2009).